Daniel B. Araya
Aerospace Laboratories,
California Institute of Technology,
Pasadena, CA 91125
e-mail: daniel.b.araya@gmail.com

Frans H. Ebersohn
Aerospace Engineering Department,
University of Michigan,
Ann Arbor, MI 48109
e-mail: febersohn@gmail.com

Steven E. Anderson[1]
Aerospace Engineering Department,
Texas A&M University,
College Station, TX 77843
e-mail: ande.ste88@gmail.com

Sharath S. Girimaji
Professor
Aerospace Engineering Department,
Texas A&M University,
College Station, TX 77843
e-mail: girimaji@tamu.edu

Magneto-Gas Kinetic Method for Nonideal Magnetohydrodynamics Flows: Verification Protocol and Plasma Jet Simulations

In this work, the gas-kinetic method (GKM) is enhanced with resistive and Hall magnetohydrodynamics (MHD) effects. Known as MGKM (for MHD–GKM), this approach incorporates additional source terms to the momentum and energy conservation equations and solves the magnetic field induction equation. We establish a verification protocol involving numerical solutions to the one-dimensional (1D) shock tube problem and two-dimensional (2D) channel flows. The contributions of ideal, resistive, and Hall effects are examined in isolation and in combination against available analytical and computational results. We also simulate the evolution of a laminar MHD jet subject to an externally applied magnetic field. This configuration is of much importance in the field of plasma propulsion. Results support previous theoretical predictions of jet stretching due to magnetic field influence and azimuthal rotation due to the Hall effect. In summary, MGKM is established as a promising tool for investigating complex plasma flow phenomena.
[DOI: 10.1115/1.4030067]

1 Introduction

Plasma flows abound in nature and engineering applications. The inherent complexity of such flows, involving transport of mass, momentum, and energy coupled with magnetic and electric fields, renders analytical approaches intractable when applied to practical engineering problems. Even, computational approaches become feasible only when restricting simplifications are invoked. The objective of the current work is to build toward a robust computational capability to simulate plasma flows for a variety of applications including MHD turbulence [1,2], MHD flow control [3], astrophysical flows [4], and particularly space propulsion [5–8]. Many current MHD numerical schemes do not simultaneously account for rarefaction effects and nonideal MHD behavior, which are dominant in the expansion of plasma jets into a vacuum. To address this need, a computational scheme is proposed that is capable of capturing the effects of noncontinuum flow as well as finite plasma conductivity and finite ion Larmor radii. It is important that these components are developed, verified, and validated individually before being combined into a single computational capability. In this paper, we incorporate nonideal MHD effects to a GKM computational fluid platform leading to the MGKM approach. In a separate paper, a unified rarefied-continuum GKM scheme is developed and validated over a wide range of Knudsen numbers.

Coupling plasma equations with a kinetic scheme offer important advantages over a conventional MHD flow solver based on the Navier–Stokes equations. Especially in highly compressible flows, a high degree of flow fidelity can be achieved near shocks as GKM is known to capture Burnett and higher-order effects [9].

Further, GKM obtains fluxes directly from the particle distribution function precluding the need for a constitutive relationship. Some thermochemical nonequilibrium effects can also be accommodated in the GKM formulation. While MGKM is motivated by space propulsion application, it can be of much value in other areas of study such as astrophysical flows, magnetic plasma confinement, and magnetic reconnection.

The objective of this work is twofold: (1) formulate MGKM to include nonideal MHD effects with a clear protocol to verify each of the individual effects; and (2) perform exploratory simulations of propulsive jets. For the verification step, we use various available analytical, computational, and experimental results in 1D and 2D benchmark flows. For the second step, experimental jet data are not readily available. Therefore, the results are examined for qualitative trends of the influence of magnetic field and Hall effects.

2 Method Development

In this section, we provide a brief overview of the basic GKM and discuss the enhancements to include nonideal MHD effects.

2.1 Overview of GKM. At its core, GKM [10,11] is a finite-volume numerical scheme for solving the Navier–Stokes equations. It is a hybridization of fluid and kinetic methods originally developed for shock capturing in high Mach number flows, but has since been shown to be effective even at weakly compressible limits [12]. The "fluid" aspect of the method involves the macroscopic properties as cell volume-averaged quantities that are evolved in time by computing fluxes at cell interfaces. The "kinetic" feature of the method is related to how these fluxes are calculated, which is by explicitly taking moments of a particle distribution function. The full derivation of the numerical scheme for solving the Navier–Stokes equations by the GKM is given by Xu [11]. In general, there are three stages to the method, which

include reconstruction, gas evolution, and projection. The governing equation for GKM can be written as the following:

$$\frac{\partial}{\partial t}\int\begin{pmatrix}\rho\\\rho\mathbf{U}\\E\end{pmatrix}d\Omega + \oint\begin{pmatrix}\mathbf{F}_\rho\\\mathbf{F}_{\rho\mathbf{U}}\\\mathbf{F}_E\end{pmatrix}\cdot d\mathbf{A} = 0 \qquad (1)$$

Equation (1) is simply the finite-volume formulation of the general conservation laws, where a macroscopic property (i.e., density ρ, momentum $\rho\mathbf{U}$, and energy E) in a control volume (Ω) changes in time due to a given flux ($\mathbf{F}$) through the control volume surface (A). During the reconstruction stage, the values of the cell-center macroscopic variables are used to create piecewise-continuous functions of these variables for all of the cells in a given computational domain. In other words, the cell-centered values are extrapolated and connected to other cell centers in a piecewise-continuous manner using limiters. For this step, the MGKM code utilizes the weighted essentially nonoscillatory limiter, which is commonly used in shock capturing schemes [13].

The gas evolution stage, wherein the intercell fluxes are calculated, represents the true kinetic aspect of GKM. For simplicity, only the 1D formulation is presented here, i.e., in the U_1-direction; however in three dimensions, the fluxes are calculated in a similar manner (see, e.g., Ref. [13]). The flux in density F_ρ, momentum $F_{\rho U_1}$, and energy F_E across the $i+1/2$ cell interface is given by

$$\begin{pmatrix}F_\rho\\F_{\rho U_1}\\F_E\end{pmatrix} = \int_{-\infty}^{\infty}u_1\begin{pmatrix}1\\u_1\\\frac{1}{2}(u_1^2+\xi^2)\end{pmatrix}f(x_{i+(1/2)},t,u_1,\xi)d\Xi \qquad (2)$$

where $d\Xi = du_1 d\xi$ is the volume element in phase space, U_1 is the macroscopic fluid velocity, and u_1 is the microscopic particle velocity. The variable ξ represents the molecular internal degrees of freedom and is specific to a particular gas depending on the ratio of specific heats. The nonequilibrium particle distribution function, f, is explicitly evaluated at the cell interface by approximating the integral solution to the Boltzmann Bhatnagar–Gross–Krook equation, which at the $i+1/2$ cell interface is given as the following:

$$f(x_{i+(1/2)},t,u_1,\xi) = \frac{1}{\tau}\int_0^t g(x_1',t',u_1,\xi)e^{-(t-t')/\tau}dt' + e^{-t/\tau}f_0(x_{i+(1/2)}-u_1 t) \qquad (3)$$

In Eq. (3), τ is the collisional relaxation time, and the only unknowns are g, which is the equilibrium distribution function, and f_0, which is the initial gas distribution function at the beginning of each time step. It can be shown that both g and f_0 can be uniquely approximated from the macroscopic variables on both the left and right sides of the cell interface. Once f has been updated, Eq. (2) is used to calculate the fluxes, and Eq. (1) is used in the projection stage to update the cell-center macroscopic values. For the 1D case, the macroscopic variables at time step $n+1$ are updated as follows:

$$\begin{pmatrix}\rho\\\rho U_1\\E\end{pmatrix}^{n+1} = \begin{pmatrix}\rho\\\rho U_1\\E\end{pmatrix}^n - \frac{1}{x_{i+(1/2)}-x_{i-(1/2)}}$$
$$\times \int_t^{t+\triangle t}\left[\begin{pmatrix}F_\rho\\F_{\rho U_1}\\F_E\end{pmatrix}_{i+(1/2)} - \begin{pmatrix}F_\rho\\F_{\rho U_1}\\F_E\end{pmatrix}_{i-(1/2)}\right]dt \qquad (4)$$

2.2 Extension to MHD.
The MHD conservation equations for mass, momentum, and energy are

$$\frac{\partial \rho}{\partial t} + \nabla \cdot (\rho\mathbf{U}) = 0 \qquad (5)$$

$$\frac{\partial(\rho\mathbf{U})}{\partial t} + \nabla \cdot \left[\rho\mathbf{U}\otimes\mathbf{U} + \underline{\underline{\Phi}} + \underline{\underline{I}}p\right] = \mathbf{J}\times\mathbf{B} \qquad (6)$$

$$\frac{\partial E}{\partial t} + \nabla \cdot \left[\mathbf{U}(E+p) - k\nabla T + \mathbf{U}\cdot\underline{\underline{\Phi}}\right] = \mathbf{J}\cdot\mathbf{E} \qquad (7)$$

In Eqs. (6) and (7), $\underline{\underline{\Phi}}$ is the viscous stress tensor, $E = \rho U^2/2 + p/(\gamma-1)$ is the hydrodynamic energy, $\mathbf{J}$ is the current density, $\mathbf{E}$ is the electric field, and $\mathbf{B}$ is the magnetic field. Note that in the absence of an electromagnetic field, Eqs. (5)–(7) reduce to the general conservative form of the hydrodynamic equations. To close these equations, the generalized Ohm's law, derived from the electron equation of motion, is used and is given as

$$\mathbf{E} = -\mathbf{U}\times\mathbf{B} + \frac{1}{n_e e}\mathbf{J}\times\mathbf{B} - \frac{1}{n_e e}\nabla(n_e k T_e) + \eta\mathbf{J} \qquad (8)$$

In Eq. (8), $\mathbf{U}\times\mathbf{B}$ is the convective term appearing in the ideal MHD equations, $\eta\mathbf{J}$ is the resistive term with η as the plasma electrical resistivity, $1/(n_e e)\mathbf{J}\times\mathbf{B}$ is the Hall term, and $1/(n_e e)\nabla(n_e k T_e)$ is the electron pressure term. Note that here e represents the elementary unit of charge, n is the number density, k is the Boltzmann constant, and T_e is the electron temperature. Implicit in the above generalized Ohm's law is the assumption that the electron time scales are fast compared to all other processes and that electron mass is negligible. Equations (5)–(8) can be rewritten to eliminate the electric field by taking the curl of Eq. (8) and making use of Faraday and Ampère's laws. If we also neglect the contribution due to the electron pressure term, the result is the following set of nonideal MHD equations that are solved by the MGKM scheme:

$$\frac{\partial \rho}{\partial t} + \nabla \cdot (\rho\mathbf{U}) = 0 \qquad (9)$$

$$\frac{\partial(\rho\mathbf{U})}{\partial t} + \nabla \cdot \left[\rho\mathbf{U}\otimes\mathbf{U} + \underline{\underline{\Phi}} + \underline{\underline{I}}p\right] = \left(\frac{\nabla\times\mathbf{B}}{\mu_0}\right)\times\mathbf{B} \qquad (10)$$

$$\frac{\partial E}{\partial t} + \nabla \cdot \left[\mathbf{U}(E+p) - k\nabla T + \mathbf{U}\cdot\underline{\underline{\Phi}}\right] = \frac{\nabla\times\mathbf{B}}{\mu_0}\cdot\left(\frac{\nabla\times\mathbf{B}}{\mu_0\sigma} - \mathbf{U}\times\mathbf{B}\right) \qquad (11)$$

$$\frac{\partial\mathbf{B}}{\partial t} = \nabla\times\left(\mathbf{U}\times\mathbf{B} - \frac{\nabla\times\mathbf{B}}{\sigma\mu_0} - \frac{(\nabla\times\mathbf{B})\times\mathbf{B}}{n_e e\mu_0}\right) \qquad (12)$$

Equation (12) is known as the magnetic field induction equation and governs the evolution of the magnetic field. Note that $\sigma = 1/(\mu_0\eta)$ is the electrical conductivity and that the addition of the nonideal MHD terms affects both the magnetic field evolution equation (12) and the energy conservation equation (11).

It has been demonstrated that the GKM scheme may be extended for ideal MHD flows, using the same gas-kinetic flux splitting method as in non-MHD flows [14–16]. However, there is no straight-forward way to extend this gas-kinetic flux splitting method to include nonideal MHD effects due to the lack of corresponding microscopic equations [15]. One alternative is to treat the magnetic terms as source terms in the governing fluid equations. Fuchs et al. [17] approached solving the ideal MHD equations in such a way by the use of the "physical" splitting of the ideal MHD equations into a "hydrodynamic and a magnetic" part. In their work, this splitting allowed the freedom to compare
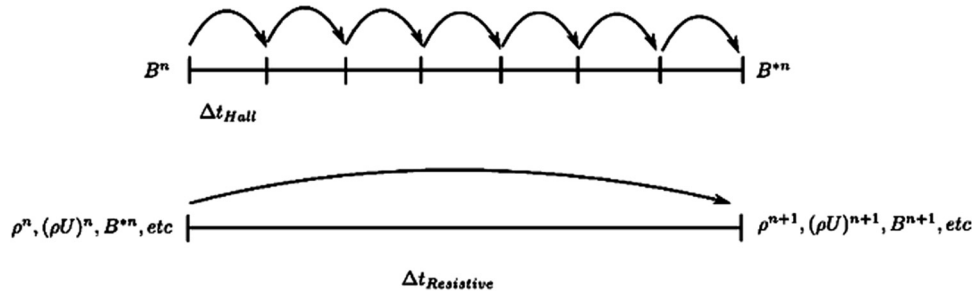
Fig. 1 Diagram of Hall term subcycling implementation

different combinations of finite-volume schemes for the mass, momentum, and energy equations and the induction equation independently.

In the present work, we follow the approach of Fuchs et al. [17] and solve the nonideal MHD equations by separating them into hydrodynamic and magnetic parts. The hydrodynamic part to be solved includes the left-hand side of Eqs. (9)–(11). Added to this are the terms on the right-hand side of Eqs. (9)–(11) as well as Eq. (12). The terms involving the magnetic field are treated as source terms and are evaluated at each time step by a central finite-difference scheme. The source term contributions are then added to the macroscopic variables during the projection stage of the previously outlined GKM scheme to update the cell-center values of ρ, $\rho\mathbf{U}$, and E. Additionally, the magnetic field $\mathbf{B}$ is evolved in time in the projection stage by the same Euler time integration scheme as the other macroscopic variables. Thus in the MGKM scheme, the governing equation is a slightly modified version of Eq. (1) to include the addition of source terms and can be written as follows:

$$\frac{\partial}{\partial t}\int \begin{pmatrix} \rho \\ \rho\mathbf{U} \\ E \\ \mathbf{B} \end{pmatrix} d\Omega + \oint \begin{pmatrix} \mathbf{F}_{\rho} \\ \mathbf{F}_{\rho\mathbf{U}} \\ \mathbf{F}_E \\ 0 \end{pmatrix} \cdot d\mathbf{A} = \begin{pmatrix} 0 \\ S_{\rho\mathbf{U}} \\ S_E \\ S_{\mathbf{B}} \end{pmatrix} \tag{13}$$

where $S_{\rho\mathbf{U}}$, S_E, and $S_{\mathbf{B}}$ are the magnetic source terms computed by a central finite-difference scheme. It should be noted that the finite-difference scheme must be compatible with the finite-volume grid. The reconstruction and gas evolution stages of the MGKM scheme are unaltered by the method outlined above. Once the density, momentum, and energy are updated, the piecewise reconstruction and fluxes are calculated in the same manner as previously outlined for the original GKM scheme.

2.2.1 Discretization and Subcycling. The discretization of the magnetic source terms on the right-hand side of Eqs. (10) and (11) is accomplished with a central differencing scheme, e.g.,

$$\frac{\partial B_x(x_i, y_j, z_k)}{\partial x} = \frac{B_x(x_{i+1}, y_j, z_k) - B_x(x_{i-1}, y_j, z_k)}{2\Delta x} \tag{14}$$

The temporal discretization of the induction equation is first-order explicit Euler, e.g.,

$$\mathbf{B}^{n+1} = \mathbf{B}^n + \left(\frac{\partial \mathbf{B}}{\partial t}\right)^n \Delta t \tag{15}$$

where $\partial\mathbf{B}/\partial t$ is given by Eq. (12).

It is important to note that the inclusion of the Hall term in the generalized Ohm's law introduces the fast-moving Whistler wave characteristic, which increases the required computational effort to resolve the fast timescale. The current approach is to isolate Hall term contributions to a separate subroutine, which is

solved on its own time scale, a process known as subcycling [18]. Figure 1 gives a graphical representation of this subcycling scheme. Note that the contributions external to the Hall subroutine are assumed to be time-invariant on the Whistler wave timescale. Such time-splitting is valid due to the large difference between the timescales of the Hall effect and flow physics.

The number of Hall subiterations per fluid iteration is determined by comparing the Whistler wave characteristic with the other characteristics of the flow. Negligible differences in results and significant decrease in overall computational effort are obtained when compared to results of very small time step simulations without subcycling. The increased computational efficiency is demonstrated in Figs. 2 and 3. The time per iteration is the time taken for the global time step, while the "equivalent time" is the time taken per subcycling iteration. This "equivalent time step" is introduced for subcycling calculations and is found by dividing the global time step by the number of subiterations. While it is still computationally more expensive to include the Hall term than not, subcycling offers significant gains for cases where Hall effects are of interest. Figure 3 shows the speedup achieved when comparing computations without subcycling to computations with subcycling in which the time step and equivalent time step for the respective computations are equal. Speedup is defined here as the total simulation time without subcycling divided by the total simulation time with subcycling.

2.2.2 Possible Errors in $\nabla \cdot \mathbf{B}$. Currently, MGKM does not employ an explicit scheme to impose the constraint $\nabla \cdot \mathbf{B} = 0$. It can be shown that the electromagnetic forces in the momentum
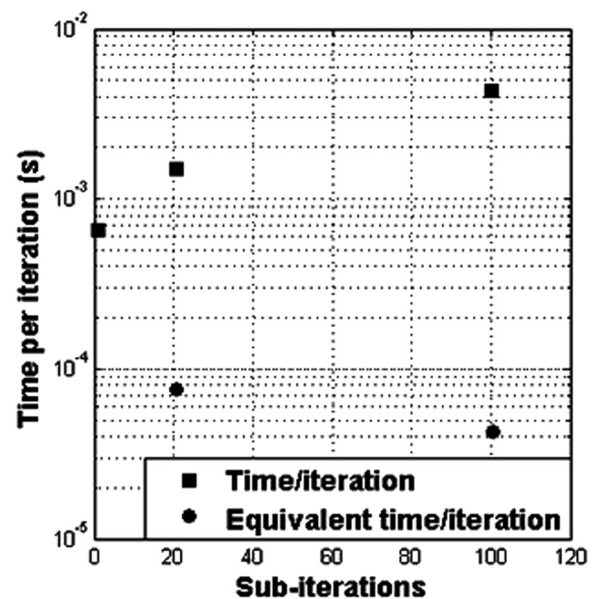

Fig. 2 Time per iteration and equivalent time per iteration with subcycling
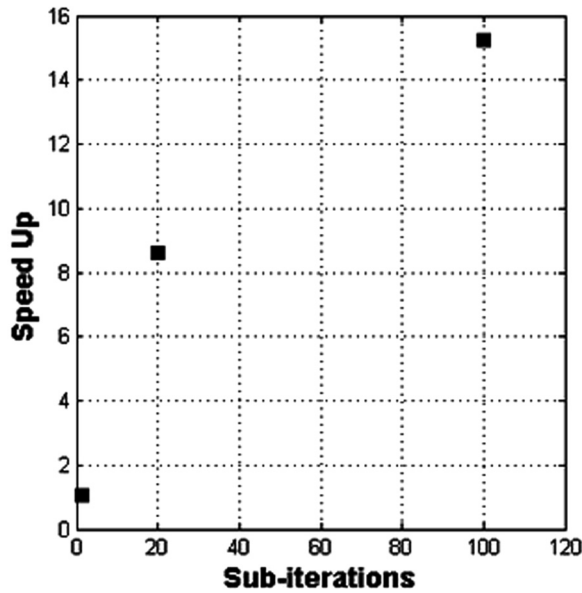
Fig. 3 Speedup with subcycling

evolution equation (the right-hand side of Eq. (10)) have a non-zero component parallel to **B** [19]

$$\mathbf{F}_{\mathrm{mag}} \cdot \mathbf{B} = (\mathbf{B} \cdot \mathbf{B})\nabla \cdot \mathbf{B} \qquad (16)$$

Thus, nonzero $\nabla \cdot \mathbf{B}$ will result in the introduction of spurious forces, which may produce unphysical results.

However, Tóth [20] has shown that the divergence-free condition can be accomplished indirectly by a suitable choice of numerical discretization. Specifically, given a divergence-free magnetic field, the central difference scheme implemented in MGKM conserves $\nabla \cdot \mathbf{B} = 0$ up to truncation error. Any additional error in enforcing this constraint is due to an imperfect initial or boundary value discretization. It is shown in Sec. 3.4 that this error can be controlled to the desired level by suitable grid and time step refinement. Thus, with sufficiently small grid sizes and time steps in MGKM, the error in $\nabla \cdot \mathbf{B}$ should not lead to unphysical results. A detailed assessment of $\nabla \cdot \mathbf{B}$ errors in the present work is given in Sec. 3.4, and further development of error mitigation schemes in future implementations of the MGKM are discussed in Sec. 4.1.

3 Results and Validation

The MGKM solver is now examined for incompressible and compressible flows in ideal, resistive, and Hall MHD regimes. First, we propose a verification and validation sequence of studies, shown in Table 1. Then, following this sequence, comparison with analytical solutions, theoretical predictions, and available experimental data are made to assess the MGKM scheme.
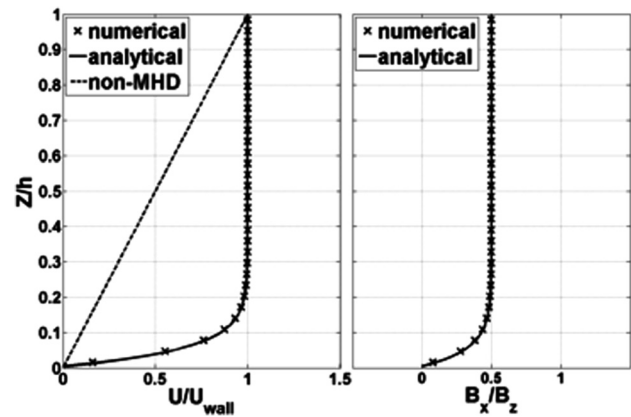

Fig. 4 Computations of MHD Couette flow. Profiles shown are the normalized velocity, U/U_{wall} (left), and induced magnetic field, B_x/B_z (right), versus normalized channel height, Z/h.

3.1 Incompressible MHD Flows–Channel Flows. MHD channel flow problems are useful benchmarks due to the existence of analytical solutions for ideal and resistive MHD flows [21]. Channel flows remain a topic of interest because of their relevance to topics such as power generation, flow acceleration, pumps, and aerodynamic heating [22–27]. Within the more complex Hall MHD regime, only semi-analytical and computational solutions exist [21,28]. In this section, MGKM results are compared with these available solutions. The nondimensional parameters used for comparison are Mach number (M), Reynolds number (R_e), Hartmann number (H_a), and magnetic Reynolds number ($R_{e,m}$)

$$M = \frac{U_c}{\sqrt{(\gamma R T)}} \qquad R_e = \frac{\rho U_c L}{\mu}$$

$$H_a = B_0 L \sqrt{\frac{\sigma}{\mu}} \qquad R_{e,m} = \mu_0 \sigma U_c L$$

Here, U_c is the characteristic flow velocity, L is the characteristic length, B_0 is the characteristic magnetic field strength, and σ is the electrical conductivity. In particular, H_a is a ratio of the magnetic to viscous forces acting on the fluid, and $R_{e,m}$ is a ratio comparing the effect of magnetic advection to that of magnetic diffusion.

In Couette flow (case 1.1), a fluid medium between two parallel walls is driven by one of the walls moving at a constant velocity. In the case of MHD Couette flow, the fluid is electrically conducting and a uniform magnetic field is applied perpendicular ($\hat{z}$) to the walls. Once the flow reaches a steady state, there exists an analytical solution for both the velocity and induced magnetic field as given by Sutton and Sherman [21]. Here, the characteristic length is the channel height ($L = h$), and the characteristic velocity is the speed of the driving wall ($U_c = U_w$). Figure 4 shows the final steady state result for a flow with M = 0.1, $R_e = 40$, $H_a = 20$, and $R_{e,m} = 10$. The channel is assumed to be infinite in the spanwise ($\hat{y}$) and streamwise ($\hat{x}$) directions, and periodic boundary

Table 1 Validation sequence and protocol

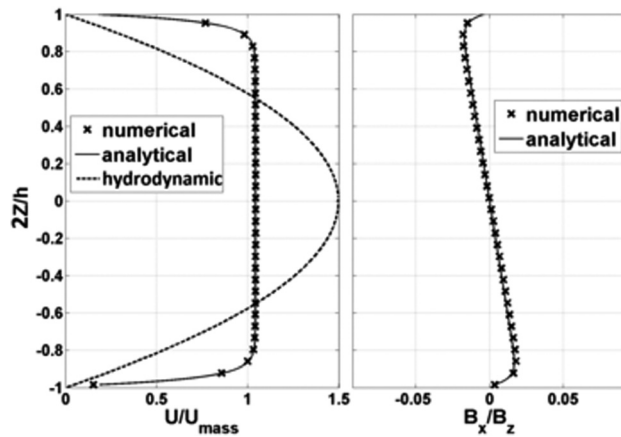| Type of flow	Case	Motivation
Incompressible channel flows	1.1—MHD Couette flow 1.2—Hartmann flow 1.3—Hall Hartmann flow	• Existence of analytical solutions • Demonstrate appropriate solution of 1D/2D resistive/Hall MHD problems • Demonstrate capability for incompressible MHD flows
Compressible shock tube	2.1—Ideal MHD shock tube 2.2—Hall MHD shock tube	• Demonstrate capability to solve compressible ideal/Hall MHD flows
Incompressible MHD jets	3.1—MHD jet stretching 3.2—Hall MHD jet rotation	• Demonstrate capability with complex 3D MHD flows of interest

Fig. 5 Computations of Hartmann flow. Profiles shown are the normalized velocity, U/U_{wall} (left), and induced magnetic field, B_x/B_z (right), versus the normalized channel height, $2Z/h$.

Fig. 7 Setup of the 1D MHD shock tube

conditions are used. The primary effect on the flow is induced by the magnetic field through the $\mathbf{J} \times \mathbf{B}$ term, which tends to force out the lower portion of the profile, filling the entire channel. In these figures, MGKM is shown to agree reasonably well with analytical solutions for both the steady state velocity and induced magnetic field profiles. Computations performed with other parameter values show similar agreement.

Hartmann flow (case 1.2) is the MHD analog to Poiseuille flow, in which a fluid is driven between stationary parallel walls by a constant streamwise pressure gradient. In Hartmann flow, the fluid is electrically conducting and a uniform magnetic field is applied perpendicular ($\hat{z}$) to the walls. Hartmann flows within the resistive MHD regime have an analytical solution [21], while Hall MHD Hartmann flows have only a semi-analytical solution [28]. Here, the characteristic length is half the channel height ($L = h/2$) and the characteristic velocity is the average flow velocity ($U_c = U_{mass}$), where $U_{mass} = (1/h) \int_0^h U(z)dz$. The channel is assumed to be infinite in the spanwise ($\hat{y}$) direction and periodic boundary conditions are employed. An inflow velocity profile is applied at one end of the channel. The computational domain is finite in the streamwise direction (parallel to the pressure gradient, ($\hat{x}$)), but is long enough such that the flow becomes fully developed. Figure 5 shows the final steady state solution for a case with M = 0.004, R_e = 416.67, H_a = 25, and $R_{e,m}$ = 0.5. The presence of the magnetic field results in a force which reduces the velocity in the center of the channel while increasing the velocity
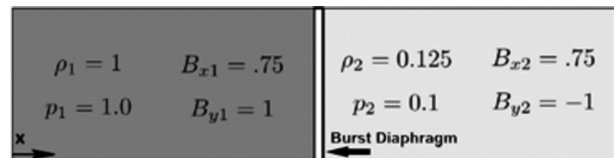
gradient near the walls. As shown, the numerical results from MGKM show acceptable agreement with the analytical solutions for both the velocity and induced magnetic field profiles. Case 1.3 studies the effect of the Hall term on the physics of Hartmann flow. The Hall parameter is given by $\alpha = \omega_{c,e}/\nu_{ei}$, where $\omega_{c,e}$ and ν_{ei} are the electron cyclotron frequency and electron–ion collision frequency, respectively. Figure 6 shows that the MGKM solver results show reasonable agreement with the semi-analytical results of Sato [28]. There are two notable features which appear due to the Hall term. First, the main flow profile is forced back toward the nonmagnetized parabolic profile. Second, the Hall term introduces a cross-flow which is transverse to the main flow.

3.2 Compressible MHD Flows–MHD Shock Tube. A shock tube is a device used to generate nearly 1D compressible flow through a pipe. If the fluid is conducting and a magnetic field is applied across the pipe, the resulting flow can be approximated using the compressible MHD equations. This is known as the MHD shock tube problem. This section presents results validating MGKM in the compressible MHD regime by applying the numerical scheme to solve the MHD shock tube problem. The MHD shock tube is setup by initially separating a high density, high pressure region from a low pressure, low density region. A current layer is applied at the diaphragm via a reversal of the initial magnetic field perpendicular to the tube axis. Figure 7 shows a schematic of the initial setup for the MHD shock tube problem.

3.2.1 Ideal MHD Shock Tube. First, numerical results for the solution of the ideal MHD shock tube problem (case 2.1) are presented. Figure 8 shows MGKM results for the density along the length of the shock tube a short time after the diaphragm has burst, along with a comparison of the results of Brio and Wu [29]. The reasonable agreement indicates that MGKM is able to capture the main features of the flow, which are the fast rarefaction and slow compound waves, the contact discontinuity, and the slow shock. Figure 9 shows the variation along the length of the tube of the velocities parallel ($\hat{x}$) and transverse ($\hat{y}$) to the tube length (U and V), the transverse magnetic field (B_y), and the pressure (P) at
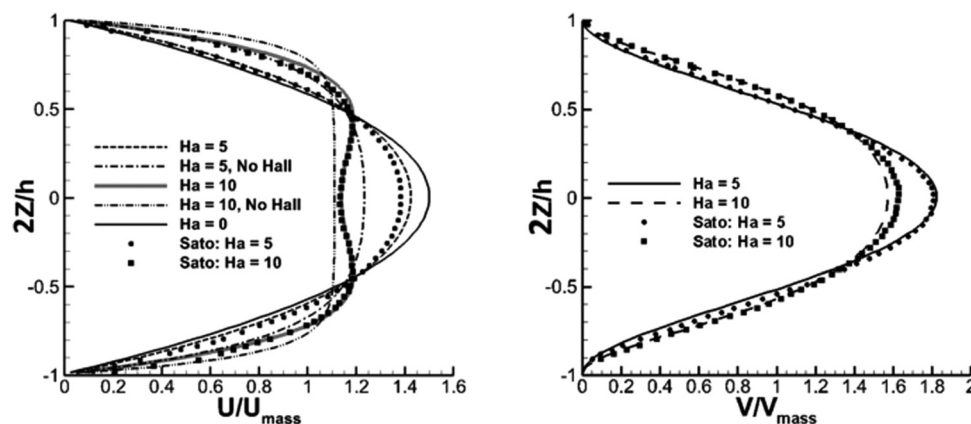

Fig. 6 Computations of Hall Hartmann flow. Comparison is made with the semi-analytical results of Sato [28]. Profiles shown are the normalized streamwise velocity, U/U_{mass} (left), and spanwise velocity, V/V_{mass} (right), versus the normalized channel height, $2Z/h$, for $\alpha = 5$.
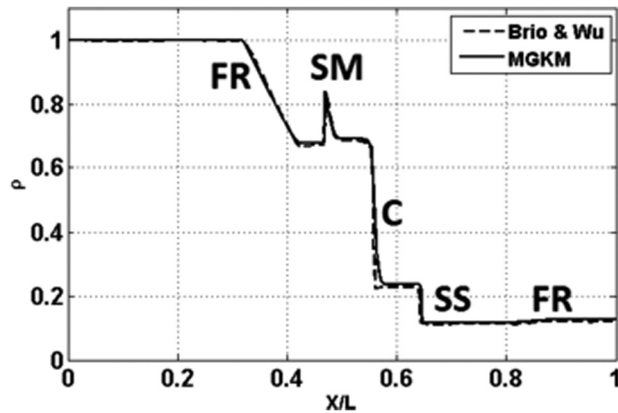
Fig. 8 Plasma density for an MHD shock tube as computed by MGKM. Comparison is made with the ideal MHD results of Brio and Wu [29].
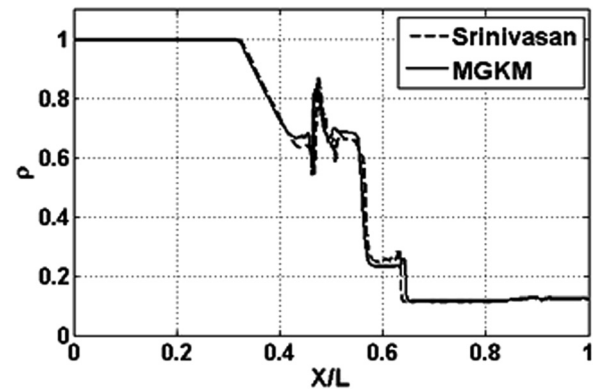

Fig. 10 Plasma density for the Hall MHD shock tube as computed by MGKM. Comparison is shown with the ideal Hall MHD results of Srinivasan [31] for nondimensional $r_L/L = 6.7 \times 10^{-4}$.

the same time instant as in Fig. 8. The results exhibit acceptable agreement. It is speculated that small disparities are possibly due to fundamental differences between the ideal (Brio and Wu) and nonideal (MGKM) schemes. The use of a first-order Euler scheme (Eq. (15)) for the discretization of Eq. (12) may also contribute to the discrepancies, which motivates the further development of a higher-order scheme as discussed in Sec. 4.1.

3.2.2 MHD Shock Tube–Hall Effects. Next, results for the Hall MHD shock tube (case 2.2) are presented. The initial conditions are the same as the previous ideal MHD case, but in this case the molar mass of the gas has been artificially raised to increase the ratio ω_f/ω_{ci}. Here, ω_f and ω_{ci} are the characteristic fluid frequency ($\omega_f \equiv U/L$) and the ion cyclotron frequency, respectively. This ratio characterizes the ratio between the Hall term and convective term in the generalized Ohm's law (8) [30].

Figure 10 compares MGKM to numerical results of Srinivasan [31]. The same general flow features appear, but disparities are present which may be due to differences between the numerical schemes. Results are further compared with those of Shumlak and Loverich [32] in Fig. 11. The simulations of Shumlak are performed with an ideal two-fluid plasma model instead of a single fluid MHD plasma model. However, MGKM shows the same general structure of the shock and exhibits qualitative agreement. Note that while the results of Srinivasan [31] and Shumlak and Loverich [32] are being compared to MGKM, there are no standard Hall MHD shock results like those of Brio and Wu for the ideal MHD shock tube.

As seen in Figs. 10 and 11, the addition of Hall physics complicates the structure of MHD shocks substantially. As the Larmor radius, r_L, increases above zero (the ideal MHD limit), the shock structure begins to develop many sharp peaks and oscillatory
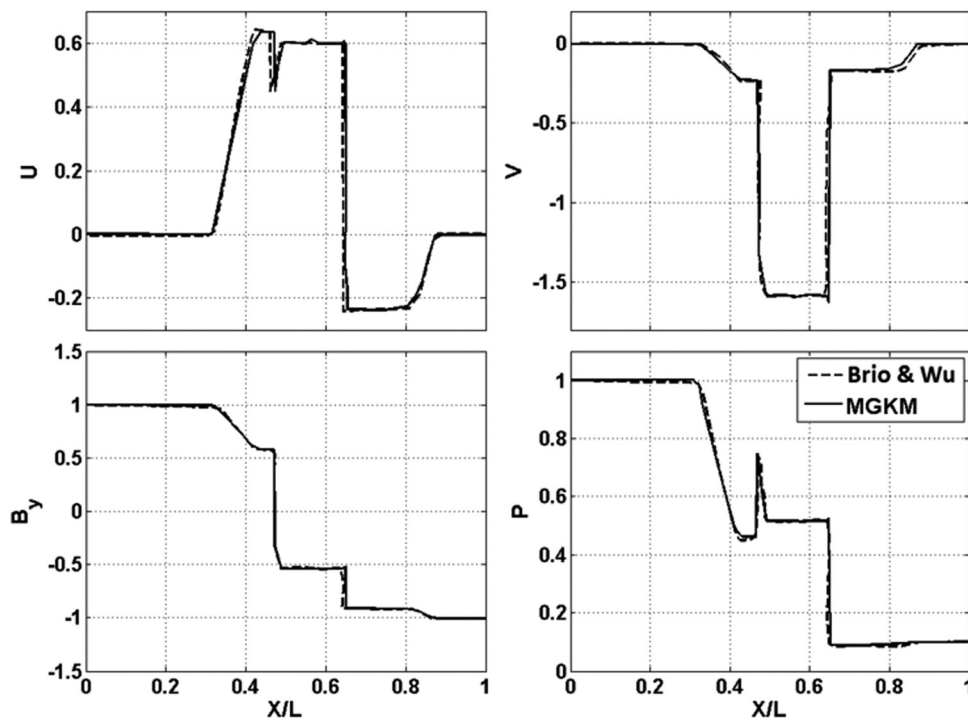

Fig. 9 MGKM computations for an MHD shock tube. Viscous/resistive results shown are the velocities parallel ($\hat{x}$) and transverse ($\hat{y}$) to the tube length (U and V), as well as the transverse magnetic field (B_y), and the pressure (P) at the same time instant as in Fig. 8. Comparison is made with the ideal MHD results of Brio and Wu [29].
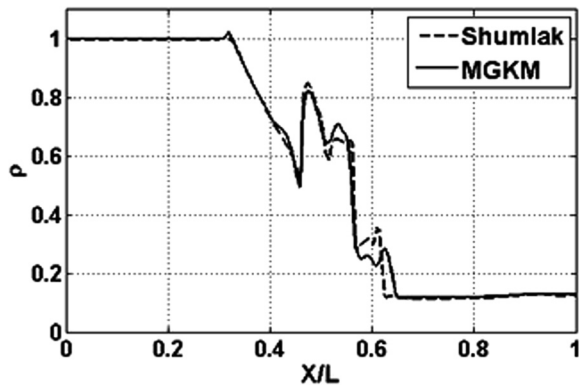
Fig. 11 Plasma density for the Hall MHD shock tube as computed by MGKM. Comparison is shown with the ideal Hall MHD results of Shumlak [32] for nondimensional $r_L/L = 3 \times 10^{-3}$.
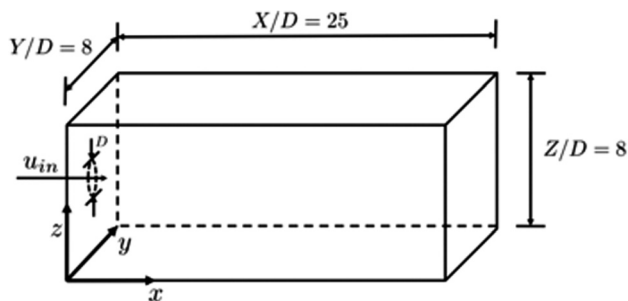

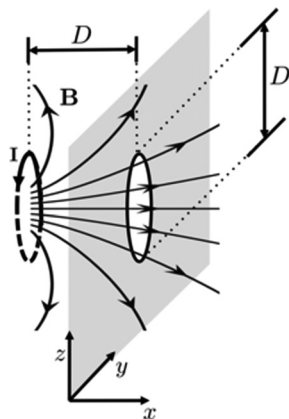**Fig. 12 Schematic of the computational domain for jet simulations**

Fig. 13 Schematic of the applied magnetic field produced by a current loop

regions. Furthermore, for large r_L, such as $r_L/L = 3 \times 10^{-3}$, the shock structure deteriorates significantly. Further study is needed to fully understand this behavior. In addition, as the Larmor radius is increased, the Hall physics introduces the Whistler wave characteristic, which significantly constrains the choice of grid size and time step [30].

3.3 Incompressible MHD Flows–MHD Jets. In this section, novel results are presented for the simulation of laminar round MHD jets under the influence of an externally applied magnetic field. The jets presented are flowing into a domain of the same density, temperature, and static pressure. The computational

Table 2 Nondimensional flow parameters for MHD jet cases

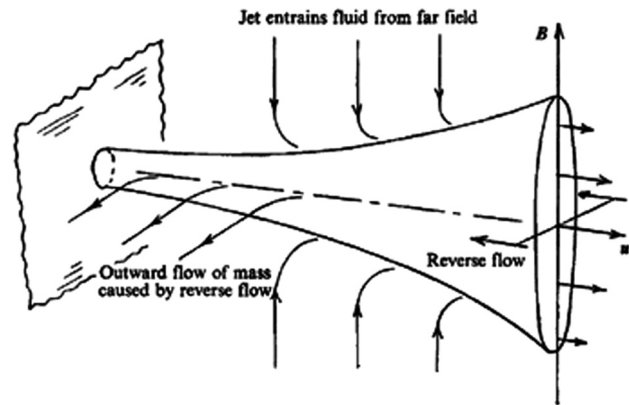| B	R_{em}	H_a	M	R_e	α
Uniform	0.103	5.13	0.129	600	—
Diverging	0.103	110	0.217	600	2.72

Fig. 14 Schematic of jet stretching from Ref. [34] along B_z, with flow reversal in the X–Y plane and outflow near the inlet

domain for the jet cases is shown in Fig. 12. All of the boundaries except the left face (Y–Z plane) have Neumann boundary conditions with zero gradients specified for all of the macroscopic flow quantities. The left face is specified as a thermally insulated wall except for the circular inlet which has a specified "plug" velocity profile. Two externally applied magnetic field configurations were studied: (1) a uniform applied magnetic field perpendicular to the flow and (2) a magnetic field generated by a current loop [30,33] as shown by the schematic in Fig. 13.

Before applying an external magnetic field to the flow, an axisymmetric laminar round jet of a conducting fluid was computed using MGKM. It was shown that without an externally applied magnetic field, the jet reaches a steady state that agrees well with the Schlichting self-similar solution for a laminar axisymmetric jet far downstream of the jet inlet [33]. Using this fully developed axisymmetric jet as the initial condition, numerical results with an externally applied magnetic field are obtained using MGKM. Qualitative comparisons are made between the resulting flow and the theoretical predictions of Davidson [34] and Gerwin et al. [35].

3.3.1 Laminar Jet Stretching. The relevant nondimensional flow parameters for the case of a uniform applied magnetic field to the fully developed axisymmetric laminar jet (case 3.1) are shown in row 1 of Table 2; they are similar to that of a liquid metal jet under the influence of a uniform magnetic field [33]. For this case, the induced magnetic field boundary condition is set to zero on the inlet plane, which is reasonable due to the small $R_{e,m}$. The computational domain is a $400 \times 128 \times 128$ Cartesian grid with grid spacing in all directions equal to $\Delta/L = 0.0025$, where Δ is the cell size and L is the characteristic domain length.

Davidson notes several features of the flow for a liquid metal jet evolving under the influence of a uniform applied magnetic field. First, the jet cross section stretches along the applied magnetic field lines due to momentum conservation and minimization of Joule dissipation that occurs by resistive heating [34]. Second, an area of reversed flow occurs next to the jet in the plane perpendicular to the applied magnetic field. This reversed flow is induced by Lorentz forces in the direction opposite of the incoming flow, which additionally leads to outflow near the plane of the jet inlet. Figure 14 shows a schematic of jet stretching along the direction
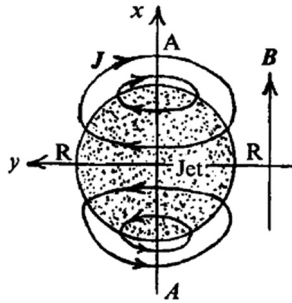
Fig. 15 Schematic of current streamlines near jet inlet from Ref. [34]

Fig. 17 Contours of the normalized streamwise velocity, U/U_{in}, at several slices in the total computational domain as computed by MGKM. Flow reversal is observed in X–Y plane.

of the applied magnetic field along with flow reversal in the X–Y midplane and outflow near the inlet. Figure 15 shows a schematic of the theoretical induced current field lines, i.e., streamlines of **J**, near the inlet of the jet. Figures 16–19 show MGKM simulation results for the MHD jet with a uniform magnetic field applied. Figure 16 demonstrates the jet stretching behavior at two different streamwise locations, where the position of the slices is normalized by the jet inlet diameter, D. Figure 17 shows where flow reversal is observed along the exterior of the jet in the plane perpendicular to the applied magnetic field. Finally, Fig. 18 shows the resulting outflow near the jet inlet to the domain, and Fig. 19 shows the induced currents in the jet. Qualitatively, these numerical results produced by MGKM seem to agree very well with Davidson's theoretical observations of resistive MHD jet behavior in the presence of a uniform applied magnetic field.
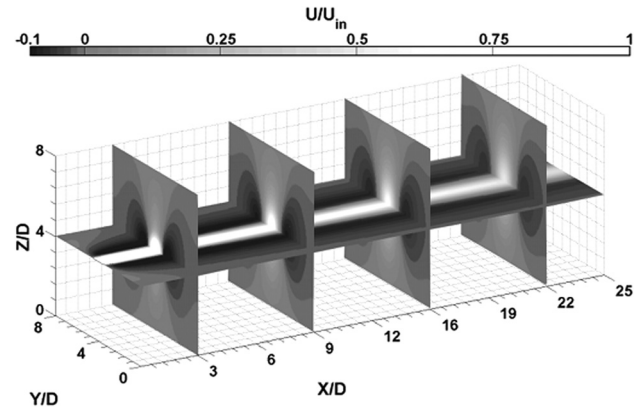
3.3.2 Plasma Jet Rotation Due to Hall Effect. The final numerical test case explores the effect of the Hall term on the behavior of MHD jets (case 3.2) [30]. In this case, the Hall term is activated in the MGKM scheme, and a strong diverging axisymmetric magnetic field is applied to the fully developed axisymmetric jet that was used in the previous test case. This case is of interest due to the important role that Hall term effects may play in magnetic nozzle physics [30]. The fluid in this simulation is similar to a Xenon plasma used in electric propulsion devices. The relevant nondimensional flow parameters for this test case are given in row 2 of Table 2. The computational domain is a
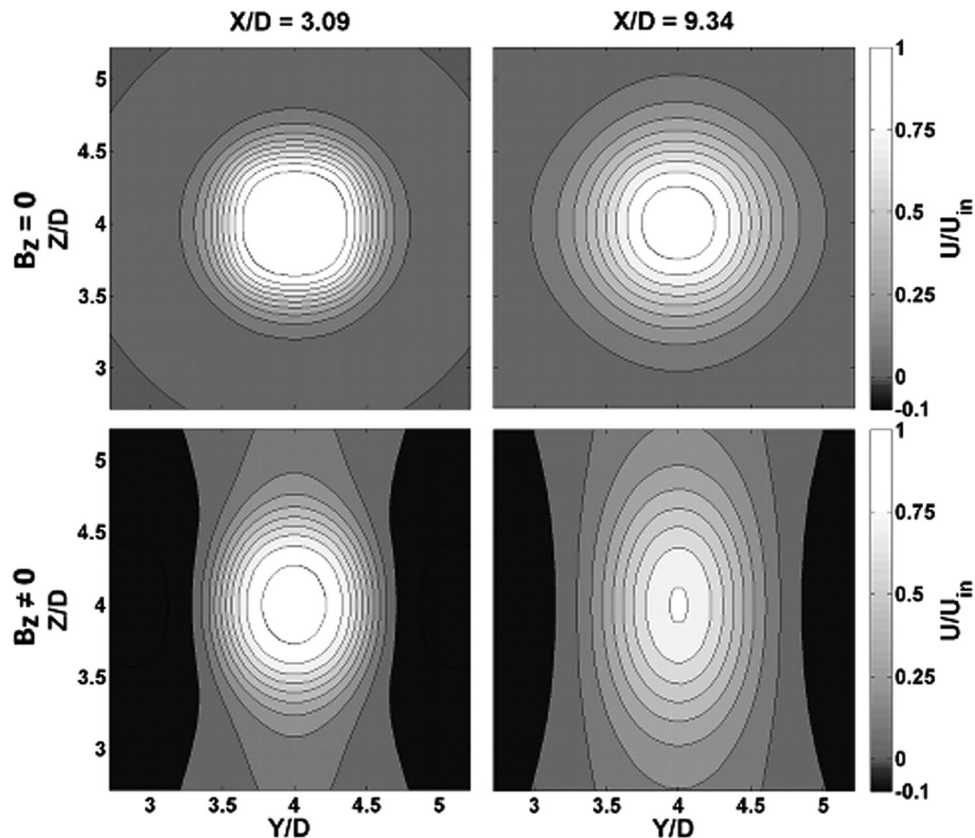

Fig. 16 Contours of the normalized streamwise velocity, U/U_{in}, in the Y–Z plane at $X/D = 3.09$ (left column) and $X/D = 9.34$ (right column) as computed by MGKM. The top row shows the jet without an external magnetic field applied, and the bottom row shows jet stretching in the direction parallel to the applied magnetic field, i.e., B_z.
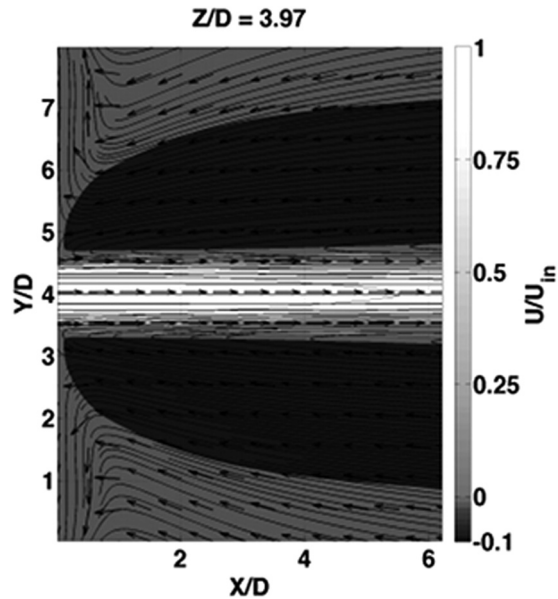
Fig. 18 Contours of normalized streamwise velocity, U/U_{in}, as computed by MGKM. Also shown are streamlines and vectors (not to scale) of the U–V components of velocity.

$200 \times 64 \times 64$ Cartesian grid with grid spacing in all directions equal to $\Delta/L = 0.005$. Gerwin predicts that the primary effect of the Hall term on a magnetic nozzle plasma jet would be to induce an azimuthal velocity [35]. The physics of the Hall term involves the demagnetization of ions, which then may travel across field lines. This can result in axial currents, producing azimuthal forces, inducing rotation in the jet. Figure 20 shows a schematic of this phenomenon. Figure 21 shows simulation results indicating axial currents and azimuthal jet velocities which develop due to Hall effects. Note that the azimuthal velocity primarily appears in the region of axial current. These axial currents result in the $\mathbf{J} \times \mathbf{B}$ force which rotates the jet. Radial currents may also develop and contribute to the rotation of the jet through interaction with the axial magnetic field.
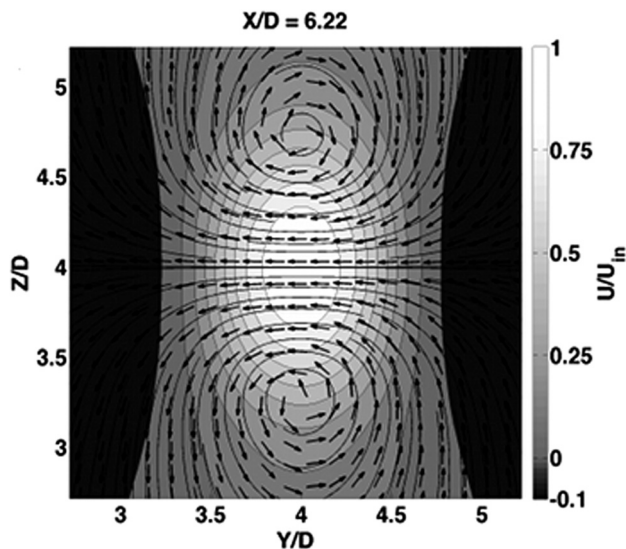

Fig. 19 Contours of normalized streamwise velocity, U/U_{in}, as computed by MGKM. Also shown are streamlines and vectors (not to scale) of the J_y–J_z components of current density.
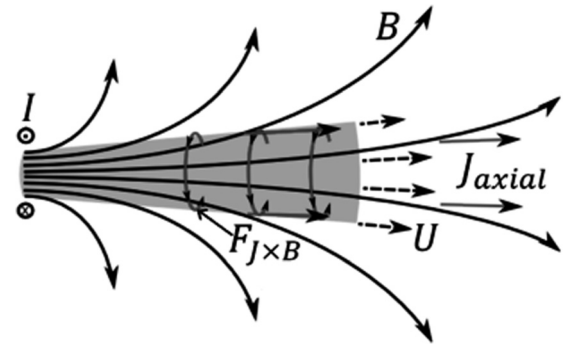

Fig. 20 Schematic of the axial currents, J_{axial}, due to Hall physics that produce azimuthal forces, $F_{J \times B}$, on the plasma jet

3.4 Observed Error in $\nabla \cdot \mathbf{B}$. This section presents a discussion of the observed errors in $\nabla \cdot \mathbf{B}$ by the MGKM solver. In our analysis of the effect of existing $\nabla \cdot \mathbf{B}$ errors, we have followed the general approach of Tóth [20], which is to compare the evolution of the primitive variables with established solutions. Sufficient agreement demonstrates that errors introduced by nonzero $\nabla \cdot \mathbf{B}$ are small enough to preclude unphysical results. Table 3 presents the volume-averaged values of $|\nabla \cdot \mathbf{B}|(L/B_0)$, which is the absolute value of $\nabla \cdot \mathbf{B}$ normalized by the characteristic magnetic field strength (B_0) and characteristic length (L) for a given problem.

For both the MHD Couette flow (case 1.1) and MHD shock tube (cases 2.1 and 2.2), the value of $\nabla \cdot \mathbf{B}$ was zero to machine precision. For all other cases, the value of volume-averaged $|\nabla \cdot \mathbf{B}|(L/B_0)$ was small, but nonzero. Notably, we observe that the error in $\nabla \cdot \mathbf{B}$ is comparable ($\approx 10^{-2}$) among Hartmann flow and plasma jet cases. The close agreement of the MGKM results for Hartmann flow with its analytical solution suggests that the effect of nonzero $\nabla \cdot \mathbf{B}$ in cases 3.1 and 3.2 is minimal and should not produce unphysical results.

Additionally, we have investigated the behavior of $|\nabla \cdot \mathbf{B}|(L/B_0)$ with respect to refinement of temporal and spatial discretization. In Fig. 22, the grid size is held constant ($\Delta x/L = 5 \times 10^{-3}$) and the time step is varied while the simulations are run out to the same total time. Similarly, in Fig. 23, the time step is held constant as the grid size is reduced and each simulation is run out to the same total time. It is important to note that the total time used in the set of grid size variation test cases is not the same as the total time used in the set of time step variation test cases. This was due to the increasing computational cost associated with refining the grid. The results indicate that refinement in either temporal resolution or spatial resolution of the simulation reduces the volume average of $|\nabla \cdot \mathbf{B}|(L/B_0)$ with respect to an equivalent total simulation time. This suggests that the implementation of the MHD equations in MGKM is consistent and that any errors in $\nabla \cdot \mathbf{B}$ that accumulate are associated with either truncation error or an imperfect initial/boundary value discretization. Thus, with sufficiently small grid sizes and time steps in MGKM, the error in $\nabla \cdot \mathbf{B}$ should not lead to unphysical results.

4 Conclusions

In this paper, a novel MGKM solver is developed for nonideal MHD flows. Resistive and Hall MHD effects are incorporated into GKM, and the MGKM solver is validated systematically against 1D and 2D ideal and nonideal MHD flows. Results agree with analytical and semi-analytical solutions for MHD Couette and Hartmann channel flows, as well as previous computational simulations of ideal and nonideal MHD shock tubes. This serves to verify the accuracy and robustness of the numerical scheme for solving complex plasma flows. Finally, novel numerical simulations of laminar round jets subject to an externally applied
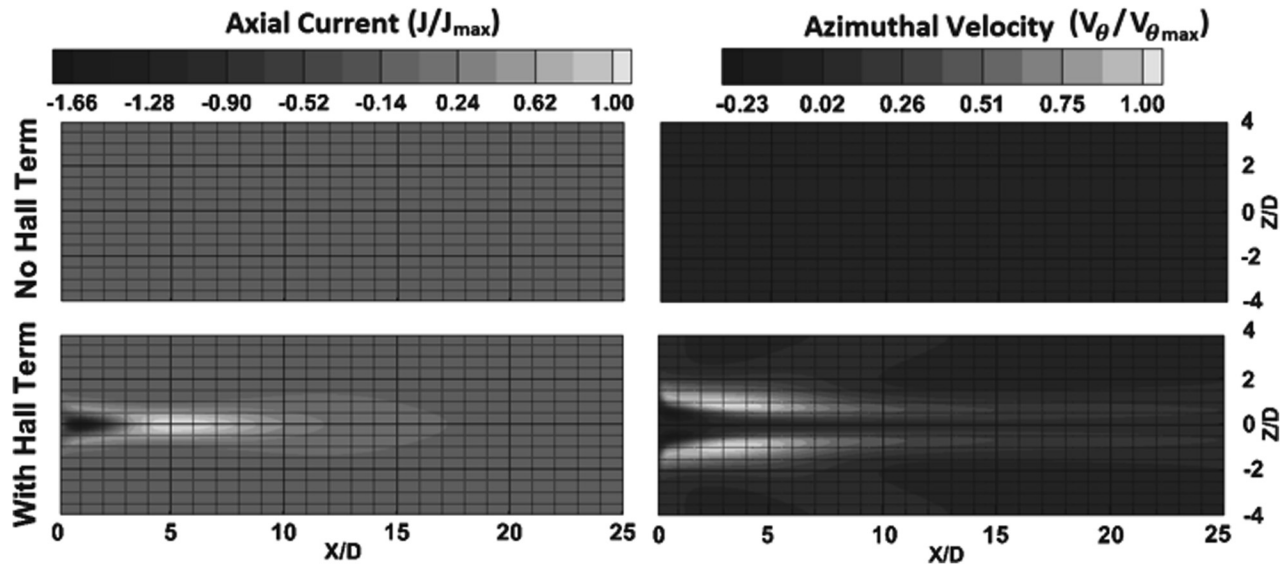
Fig. 21 Contours of normalized axial ($\hat{x}$) current density, J/J_{max}, and azimuthal ($\hat{\theta}$) velocity, $V_\theta/V_{\theta max}$, as computed by MGKM with and without the Hall term

Table 3 Volume-averaged values of $|\nabla \cdot \mathbf{B}|L/B_0$

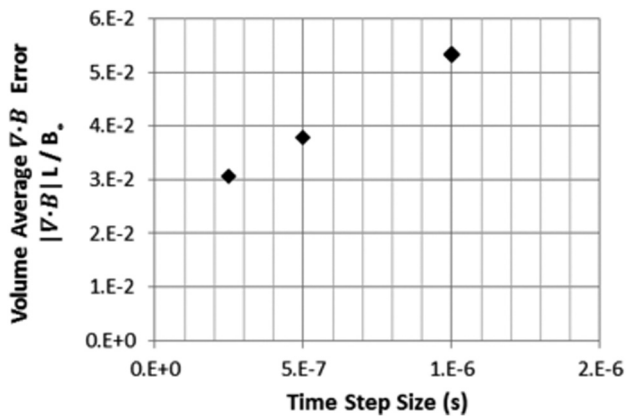| Case	1.1	1.2	1.3	2.1	2.2	3.1	3.2
$|\nabla \cdot \mathbf{B}|L/B_0$	0	1.1×10^{-2}	3.5×10^{-2}	0	0	5.4×10^{-2}	6.0×10^{-2}

Fig. 22 Normalized volume average of $\nabla \cdot \mathbf{B}$ versus Δt (s)
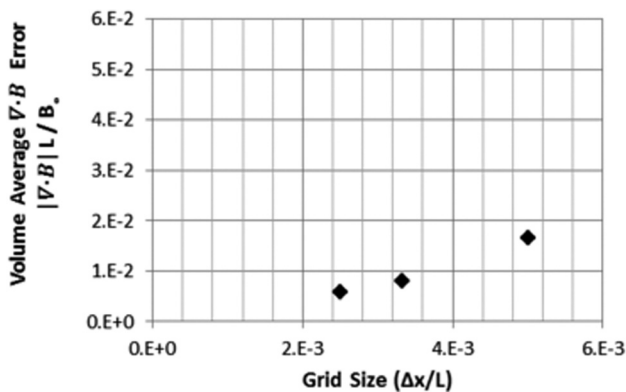

Fig. 23 Normalized volume average of $\nabla \cdot \mathbf{B}$ versus $\Delta x/L$

magnetic field are presented that incorporate both resistive and Hall MHD physics. These numerical results agree qualitatively with theoretical predictions of the resulting features of the MHD jet. Overall, MGKM exhibits encouraging potential for further development and application to practical plasma flows of interest.

4.1 Future Work. While MGKM has demonstrated capability with continuum ideal and nonideal MHD flows, it currently has some limitations. As discussed in Secs. 2.2.2 and 3.4, MGKM is susceptible to initial and boundary errors in $\nabla \cdot \mathbf{B}$. Although this can be somewhat mitigated by a careful choice of initial and boundary conditions, a more robust solver will require some additional method to eliminate inaccuracy arising from these errors. Future development of MGKM will incorporate a scheme for active mitigation of nonzero $\nabla \cdot \mathbf{B}$, such as those described by Tóth [20].

Additionally, the current implementation of MGKM requires further augmentation for solving high Knudsen number flows. Future implementations of MGKM aim to incorporate a unified rarefied-continuum GKM scheme being developed concurrently. Further, the finite-difference implementation and first-order temporal discretization of the magnetic field effects render simulations susceptible to oscillations when the Larmor radius is large. Thus, the finite-difference scheme must be improved to accommodate the physics of large Larmor radius cases. In particular, a higher-order scheme for discretization of Eq. (12) is currently being developed. Finally, the addition of complex transport properties, such as tensorial resistivity, would be especially valuable given the complex anisotropic behavior of magnetized plasmas.

Acknowledgment

References

[1] Richard, J. C., Riley, B. M., and Girimaji, S. S., 2011, "Magnetohydrodynamic Turbulence Decay Under the Influence of Uniform or Random Magnetic Fields," ASME J. Fluids Eng., 133(8), p. 081205.

[2] Shebalin, J. V., 2014, "Temperature and Entropy in Ideal Magnetohydrodynamic Turbulence," ASME J. Fluids Eng., 136(6), p. 060901.

[3] Chatterjee, D., Chatterjee, K., and Mondal, B., 2012, "Control of Flow Separation Around Bluff Obstacles by Transverse Magnetic Field," ASME J. Fluids Eng., 134(9), p. 091102.

[4] Tordella, D., Belan, M., Massaglia, S., De Ponte, S., Mignone, A., Bodenschatz, E., and Ferrari, A., 2011, "Astrophysical Jets: Insights Into Long-Term Hydrodynamics," New J. Phys., 13, p. 043011.

[5] Lorzel, H., and Mikellides, P. G., 2010, "Three-Dimensional Modeling of Magnetic Nozzle Processes," AIAA J., 48(7), pp. 1494–1503.

[6] Xisto, C. M., Páscoa, J. C., and Oliveira, P. J., 2013, "Numerical Modeling of Electrode Geometry Effects on a 2D Self-Field MPD Thruster," ASME Paper No. V001T01A051.

[7] Mikellides, P. G., Turchi, P. J., and Roderick, N. F., 2000, "Applied-Field Magnetoplasmadynamic Thrusters, Part 1: Numerical Simulations Using the MACH2 Code," J. Propul. Power, 16(5), pp. 887–893.

[8] Mikellides, I. G., Mikellides, P. G., Turchi, P. J., and York, T. M., 2002, "Design of a Fusion Propulsion System-Part 2: Numerical Simulation of Magnetic-Nozzle Flows," J. Propul. Power, 18(1), pp. 152–158.

[9] Liao, W., Peng, Y., Luo, L.-S., and Xu, K., 2008, "Modified Gas-Kinetic Scheme for Shock Structures in Argon," Prog. Comput. Fluid Dyn., 8(1–4), pp. 97–108.

[10] Xu, K., Martinelli, L., and Jameson, A., 1995, "Gas-Kinetic Finite Volume Methods, Flux-Vector Splitting, and Artificial Diffusion," J. Comput. Phys., 120(1), pp. 48–65.

[11] Xu, K., 2001, "A Gas-Kinetic Scheme for the Navier–Stokes Equations and its Connection With Artificial Dissipation and the Godunov Method," J. Comput. Phys., 171(1), pp. 289–335.

[12] Kerimo, J., and Girimaji, S., 2007, "Boltzmann-BGK Approach to Simulating Weakly Compressible 3D Turbulence: Comparison Between Lattice Boltzmann and Gas Kinetic Methods," J. Turbul., 8(46).

[13] Kumar, G., Girimaji, S., and Kerimo, J., 2013, "WENO-Enhanced Gas-Kinetic Scheme for Direct Simulations of Compressible Transition and Turbulence," J. Comput. Phys., 243, pp. 499–523.

[14] Xu, K., and Tang, H., 2000, "A High-Order Gas-Kinetic Method for Multidimensional Ideal Magnetohydrodynamics," J. Comput. Phys., 165(1), pp. 69–88.

[15] Xu, K., 1999, "Gas-Kinetic Theory-Based Flux Splitting Method for Ideal Magnetohydrodynamics," J. Comput. Phys., 153(2), pp. 334–352.

[16] Tang, H., Xu, K., and Cai, C., 2010, "Gas-Kinetic BKG Scheme for Three Dimensional Magnetohydrodynamics," Numer. Math.: Theory Meth. Appl., 3(4), pp. 387–404.

[17] Fuchs, F., Mishra, S., and Risebro, N., 2009, "Splitting Based Finite Volume Schemes for Ideal MHD Equations," J. Comput. Phys., 228(3), pp. 641–660.

[18] Huba, J., 2003, "Hall Magnetohydrodynamics—A Tutorial," Space Plasma Simulation, Springer, Berlin, pp. 166–192.

[19] Brackbill, J., and Barnes, D., 1980, "The Effect of Nonzero $\nabla \cdot B$ on the Numerical Solution of the Magnetohydrodynamic Equations," J. Comput. Phys., 35(3), pp. 426–430.

[20] Tóth, G., 2000, "The $\nabla \cdot B = 0$ Constraint in Shock-Capturing Magnetohydrodynamics Codes," J. Comput. Phys., 161(2), pp. 605–652.

[21] Sutton, G., and Sherman, A., 1965, Engineering Magnetohydrodynamics, McGraw-Hill, New York.

[22] Amano, R., Xu, Z., and Lee, C.-H., 2007, "Numerical Simulation of Supersonic MHD Channel Flows," ASME 2007 International Design Engineering Technical Conferences and Computers and Information in Engineering Conference, American Society of Mechanical Engineers, pp. 669–676.

[23] Attia, H. A., 2005, "Unsteady MHD Couette Flow and Heat Transfer Between Parallel Porous Plates With Exponential Decaying Pressure Gradient," ASME 2005 International Mechanical Engineering Congress and Exposition, American Society of Mechanical Engineers, pp. 901–905.

[24] Jiang, F., Oliveira, M. S., and Sousa, A. C., 2005, "SPH Simulations for Turbulence Control of Magnetohydrodynamic Poiseuille Flow," ASME 2005 Fluids Engineering Division Summer Meeting, American Society of Mechanical Engineers, pp. 385–394.

[25] Midya, C., Layek, G., Gupta, A., and Mahapatra, T. R., 2003, "Magnetohydrodynamic Viscous Flow Separation in a Channel With Constrictions," ASME J. Fluids Eng., 125(6), pp. 952–962.

[26] Smith, T., and Paul, P., 1979, "Radiative Transfer in Hartmann MHD Flow," ASME J. Heat Transfer, 101(3), pp. 502–506.

[27] Liu, R., Vanka, S. P., and Thomas, B. G., 2014, "Particle Transport and Deposition in a Turbulent Square Duct Flow With and Imposed Magnetic Field," ASME J. Fluids Eng., 136(12), p. 121201.

[28] Sato, H., 1961, "The Hall Effect in the Viscous Flow of Ionized Gas Between Parallel Plates Under Transverse Magnetic Field," J. Phys. Soc. Jpn., 16(7), pp. 1427–1433.

[29] Brio, M., and Wu, C., 1988, "An Upwind Differencing Scheme for the Equations of Ideal Magnetohydrodynamics," J. Comput. Phys., 75(2), pp. 400–422.

[30] Ebersohn, F., 2012, "Gas Kinetic Study of Magnetic Field Effects on Plasma Plumes," Master's thesis, Texas A&M University, College Station, TX.

[31] Srinivasan, B., 2010, "Numerical Methods for Three-Dimensional Magnetic Confinement Configurations Using Two-Fluid Plasma Equations," Ph.D. thesis, University of Washington, Seattle, WA.

[32] Shumlak, U., and Loverich, J., 2003, "Approximate Riemann Solver for the Two-Fluid Plasma Model," J. Comput. Phys., 187(2), pp. 620–638.

[33] Araya, D., 2011, "Resistive MHD Simulations of Laminar Round Jets With Applications to Magnetic Nozzle Flows," Master's thesis, Texas A&M University, College Station, TX.

[34] Davidson, P., 1995, "Magnetic Damping of Jets and Vortices," J. Fluid Mech., 229, pp. 153–185.

[35] Gerwin, R., Markin, G., Sgro, A., and Glasser, A., 1990, "Characterization of Plasma Flow Through Magnetic Nozzles," Los Alamos National Laboratory, Technical Report No. AL-TR-89-092.